

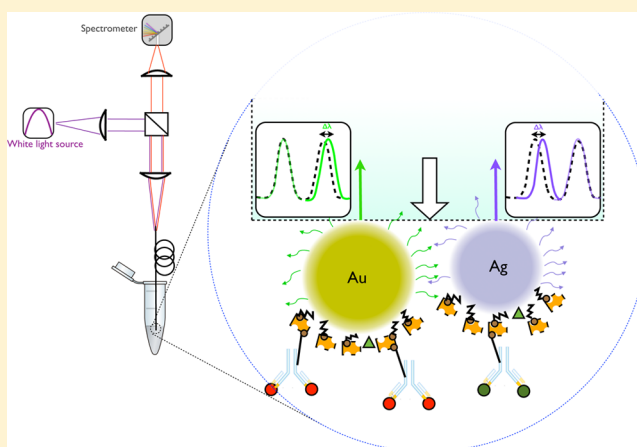
Dip Biosensor Based on Localized Surface Plasmon Resonance at the Tip of an Optical Fiber

Beniamino Sciacca* and Tanya M. Monro*

Institute for Photonics and Advanced Sensing and School of Chemistry and Physics, The University of Adelaide, Adelaide, South Australia 5005, Australia

Supporting Information

ABSTRACT: A dip biosensor is realized by depositing metallic nanoparticles onto the tip of a cleaved optical fiber. Light coupled into the fiber interacts with the localized surface plasmons within the nanoparticles at the tip; a portion of the scattered light recouples into the optical fiber and is analyzed by a spectrometer. Characterization of the sensor demonstrates an inverse relationship between the sensitivity and the number of particles deposited onto the surface, with smaller quantities leading to greater sensitivity. The results obtained showed also that by depositing nanoparticles with distinct localized surface plasmon resonance signatures with limited overlap, as for the case of gold and silver nanospheres, a multiplexed dip biosensor can be realized by simply functionalizing the different nanoparticles with different antibodies after the fashion of an immunoassay. In this way different localized surface plasmons resonance bands responsive to different target analytes can be separately monitored, as further presented below, requiring a minimal quantity of reagents both for the functionalization process and for the sample analysis.



INTRODUCTION

Biosensors are a promising alternative to expensive conventional medical diagnostic techniques commonly employed in clinical laboratories such as enzyme-linked immunosorbent assays (ELISA) or Western blots.^{1–3} Compared to such techniques, biosensors have the advantage of being cost effective, quick, and portable and therefore suitable for point-of-care testing (POCT).^{4–8} Although some specific biosensors are already present in the market, including, for example, glucose monitoring,^{9–11} they are not widely employed yet to screen biomarkers for early diagnosis of diseases.¹² Of all classes of sensing strategies, optical biosensors are a promising choice for early diagnostics, as they have the potential for low cost, rapid response, and high reliability.^{6,8,13–15} Furthermore, significant research effort is currently focused on developing multiplexed architectures to increase the number of biomarkers that could be screened simultaneously to improve the confidence interval of the analysis.^{16–20} However, for current clinical techniques such as ELISA, a major cost lies in the quantity of reagents, particularly antibodies, required to functionalize the surface.^{21,22} Although significant focus is given in the literature on ways of improving biosensor performance, little attention has been paid to date to creating sensing architectures that limit the quantity of reagents required for analysis without loss in sensitivity or specificity.

Here we present a compellingly simple *dip biosensor* architecture based on excitation of localized surface plasmons (LSP) that could address these issues.

Localized surface plasmon resonances (LSPRs) are collective electron charge oscillations in metallic nanoparticles, such as gold or silver nanoparticles (GNP or SNP, respectively), that are excited by light at the resonance wavelength.^{23–25} The LSPR frequency depends on the refractive index of the medium surrounding the nanoparticles, making it a suitable transducing mechanism for optical biosensing. By linking the nanoparticles to the tip of a cleaved optical fiber, a powerful and sensitive transduction mechanism is transformed into a miniaturized device for biosensing (see Figure 1).

Although a similar architecture has already been proposed for refractive index sensing,^{26–28} in this paper we demonstrate the importance of controlling the quantity of nanoparticles on the fiber's tip and demonstrate that with this architecture it is possible to simultaneously detect distinct gastric cancer biomarkers (*multiplexing*) in clinically relevant concentrations, making use of a minimal quantity of reagents both for the functionalization process and for sample analysis, thanks to the miniaturization achievable by employing the tips of optical

Received: September 22, 2013

Revised: January 7, 2014

Published: January 8, 2014

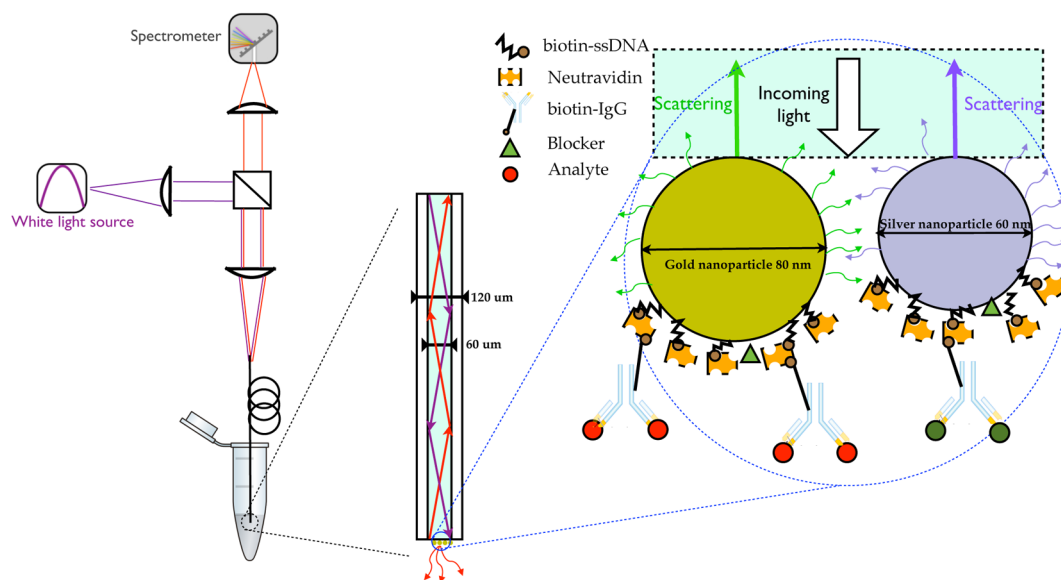


Figure 1. (Left) Optical setup of the dip sensor for analysis of the localized surface plasmon resonance of metallic nanospheres. Schematic shows the typical setup employed in this work for biosensing, highlighting the interactions at the tip of the optical fiber. (Right) Cartoon of the interaction between light and the nanospheres at the tip of the optical fiber. Some of the transmitted light interacts with the surface plasmon of gold and silver nanospheres and is partially scattered; a portion of the scattered light is recoupled into the fiber and analyzed by the spectrometer as a peak in the reflectance spectrum. The surface functionalization approach is also displayed.

fibers. In the last part of the paper, we show that by playing with the surface functionalization it is possible to drive the nanoparticles positioning and therefore their interactions. In particular, we show the difference in the LSPR shift between nanoparticles located next to each other and nanoparticles sitting on top of each other.

EXPERIMENTAL SECTION

Optical Setup and Data Processing. Light emitted by a tungsten halogen light source (HL-2000-HP, Ocean Optics) was focused and coupled into the cleaved fiber sample through a beam splitter (see Figure 1). At the cleaved interface at the other end of the fiber sample (typically 50 cm long), a fraction of traveling light is reflected back along the fiber, according to Fresnel equations. By means of a beam splitter, the reflected light is separated from the incident light and fed into a cooled compact CCD spectrometer (Ocean Optics, QE65000, SNR 1000:1). Each recorded spectrum was typically averaged over 10 s (100–200 averages, depending on the acquisition time) to reduce the noise. Data were analyzed by means of an in-house-developed Matlab routine that performs a cross-correlation between the reflectance spectra and identifies the SPR shift over time. For the multiplexed biosensor, prior to cross-correlation, the two LSPR bands were first isolated by cutting the spectrum into two parts (350–500 and 500–650 nm). The wavelength position of each band was then calculated over time by means of the aforementioned cross-correlation routine, resulting in two distinct curves, each representing the shift of a LSPR band.

Sensor Preparation and Functionalization. A commercial multimode silica optical fiber purchased from Corning 62.5/125 (core 62.5 μm , cladding 62.5 μm , NA 0.258) was cleaved and functionalized with a 2 mg/mL solution of PAH in 1 M NaCl (100 μL of solution used for several experiments) and rinsed with Millipore water. PAH is a positively charged polyelectrolyte that adsorbs onto the negatively charged glass surface, introducing amine groups to electrostatically link the metallic nanoparticles to the tip of the cleaved fiber. The PAH-terminated fiber was immersed into the GNP solution (80 nm, 0.05 mg/mL, citrate capped, nanoComposix) for 5–30 min. An emission band corresponding to the LSPR of GNP was observed at a wavelength of 545 nm (in water) (see inset of Figure 2A). The sample was then rinsed with Millipore water. The fiber

modified with GNP was then immersed in 50 mM sodium phosphate buffer (SPB, pH 6) for few minutes and in 50 mM SPB (pH 3) until a stable LSPR baseline was observed. The fiber was then placed in a 10 μM biotin–thiol single-strand DNA (ssDNA) (SH-ACAT-TAAAATCCACACACGCTAACATACACA-Biotin) solution in 50 mM SPB (pH 3) for 1 h to promote covalent binding between the thiol-terminated ssDNA and the GNP.²⁹ The fiber tip was successively rinsed in SPB (pH 3) and SPB (pH 6) until a stable position of the LSPR band was obtained. SPB (pH 6) promotes desorption of unlinked ssDNA because of the increased electrostatic repulsion between negatively charged GNP and ssDNA.³⁰ The sample was then placed in phosphate-buffered saline (PBS, pH = 7.4). The biotin-terminated GNP were exposed for about 30 min to 400 nM Neutravidin, a tetrameric protein that binds specifically biotin, previously immobilized to the fiber tip, forming a strong noncovalent bond ($K_D \approx 10^{-15}$ M).³¹ After a thorough PBS wash, the sample was further functionalized with a solution of biotinylated antiapolipoprotein E (apoE) IgG (330 nM, MabTech) for about 60 min, allowing the biotin function of antibodies to bind to free groups on Neutravidin (see Figure 1), resulting in GNP terminated with anti-apoE antibodies. A red shift of the LSPR of GNP was observed along with the functionalization, confirming a successful binding process. SNP were then linked to the fiber by placing the tip into the SNP solution (60 nm, 0.02 mg/mL, citrate capped, nanoComposix), producing a new band in the spectrum at a wavelength of 425 nm (in water), corresponding to the LSPR of SNP (see Figure 3A). Immobilization of SNP on the fiber tip typically caused a red shift of the band corresponding to GNP, as further commented in text (see Figure 3A). The same functionalization process was followed as for GNP, monitoring the two LSPR bands over time. After Neutravidin, SNP were functionalized with biotinylated anti-Clusterin (CLU) IgG (330 nM, R&D System) for about 60 min. After immobilization of antibodies, the sensor was exposed to a blocking reagent (The Blocking Solution, Candor) for 10 min in order to block unreacted binding sites, thus reducing nonspecific binding. A negligible shift of the two LSPR bands was observed after the blocking step, meaning that ssDNA self-assembly covered most of the nanosphere's surface. Protein solutions (apoE and CLU) were prepared in PBS (pH 7.4) prior to the biosensing experiments and discarded afterward.

Sodium phosphate buffer was prepared by mixing monosodium phosphate monohydrate and disodium phosphate heptahydrate at

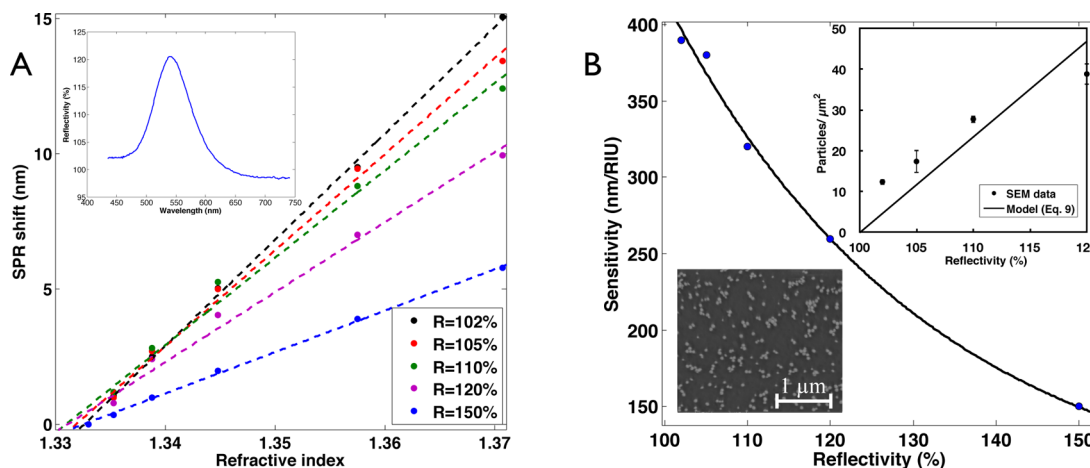


Figure 2. (A) Measured LSPR shift as a function of the refractive index for fiber samples with an increasing amount of GNP on the surface and therefore an increasing reflectivity in the measured spectrum. (Inset) Typical measured LSPR spectrum of GNP, with a reflectivity of 120%. (B) Sensitivity calculated from values in A as a function of the extra reflectivity introduced by the nanoparticles (100% of reflectivity means no nanoparticles). Larger GNP density leads to samples with smaller sensitivity. (Bottom inset) SEM micrograph taken from a fiber sample with an amount of GNP corresponding to 120% reflectivity. (Top inset) Correlation between the reflectivity of the fiber sample and the amount of GNP measured by SEM analysis; number of GNP calculated from the model in eq 9 is reported as well (solid line).

different concentrations to obtain the desired pH. In particular, for the 50 mM pH 3 SPB, the monosodium phosphate monohydrate's concentration was 6.9 g/L and the disodium phosphate heptahydrate's was 1.6 mg/L. For the pH 6 SPB, the monosodium phosphate monohydrate's concentration was 6.0 g/L and the disodium phosphate heptahydrate's was 1.6 g/L. A calibrated pH meter was used to measure the pH of the buffer.

SEM Measurements. The fiber sample was vertically mounted onto a stage for scanning electron microscopy (SEM) analysis. The instrument employed was a FEI Quanta 450 FEG Environmental Scanning Electron Microscope, and micrographs were taken at a voltage of 10 kV. Images recorded were analyzed by manually counting the number of nanoparticles within an area of $9 \mu\text{m}^2$ over the core of the fiber tip.

RESULTS AND DISCUSSION

Characterization of the GNP Sensor. The light coupled into the optical fiber reaches the cleaved interface where it interacts with the nanoparticles adsorbed on the fiber tip. A fraction of the light scattered by the nanoparticles recouples to the fiber, overlapping with the light back reflected at the fiber–water interface, and produces a LSPR signature in the spectrum collected by the spectrometer.

The spectrum that results from immersing the fiber tip in Millipore water after poly(allylamine hydrochloride) (PAH) adsorption (see Experimental Section) was used as a reference (B) for data analysis, and for convenience it will be referred to later in the manuscript to 100% of reflectivity (consistent with eq 1). The relative reflectance is calculated to be

$$R(\lambda, \%) = \frac{S(\lambda) - D(\lambda)}{B(\lambda) - D(\lambda)} \times 100 \quad (1)$$

where S is the spectrum to be analyzed and D is the *dark* signal (measured with the light source off).

We explored the performance of the sensor as a function of the quantity of nanoparticles linked to the surface in order to find the optimal conditions for the biosensing experiments.

Dip sensor performance was characterized by exposing the surface to glycerol/water solutions with refractive indices ranging from 1.33 to 1.37 and measuring the LSPR response. A cross-check of the sensitivity was performed as well by

exposing each loading condition to absolute ethanol ($n = 1.36$), and the obtained LSPR shift was in full agreement with the curves of Figure 2A (data not shown).

To reduce the number of variables, only GNP were linked to the fiber tip for this analysis. The amount of adsorbed GNP was controlled as a function of adsorption time using the real-time measure of the LSPR band intensity as feedback to eliminate artifacts arising from variations in the adsorption kinetics. Indeed, the intensity of the LSPR band could be employed as an indirect way of estimating the amount of GNP adsorbed, as further explored below. Figure 2A shows the LSPR shift as a function of refractive index, for samples coated with an increasing amount of GNP, from 102% to 150% of reflectivity of the LSPR band at the resonance wavelength. Linear fits of the data points are superimposed as well for each condition, showing clear linearity between the SPR shift and the refractive index, as previously demonstrated.^{23,32}

To provide a general comparison between different conditions, the sensitivity of the samples, calculated from the slope of the linear fits of the curves in Figure 2A, is plotted as a function of the reflectivity (amount of GNP on the surface) in Figure 2B, along with the exponential fit (solid line). Interestingly, the data shows that by increasing the amount of GNP linked to the surface (reflectivity) the sensor sensitivity is significantly compromised. The fit reported in Figure 2B has $R^2 = 0.99$, and the asymptotic value of the exponential (offset) is around 80 nm/RIU.

It is well known that as the distance between two single particles is reduced the LSPR is shifted toward the red, and this effect has been employed for plasmonic rulers.^{29,33–35} We observed a red shift of the LSPR in water as a function of the amount of GNP loaded on the fiber, which is a measure of the degree of plasmonic coupling between the nanoparticles. However, as shown in Figure 2B, larger GNP density leads to smaller sensitivity. We believe that the reason for this degradation in performances could be attributed to a decrease of the effective refractive index surrounding the GNP. In fact, as the loading increases, GNP get closer together and the effective refractive index, averaged between that of the medium and that of gold, decreases, being the real part of the gold refractive

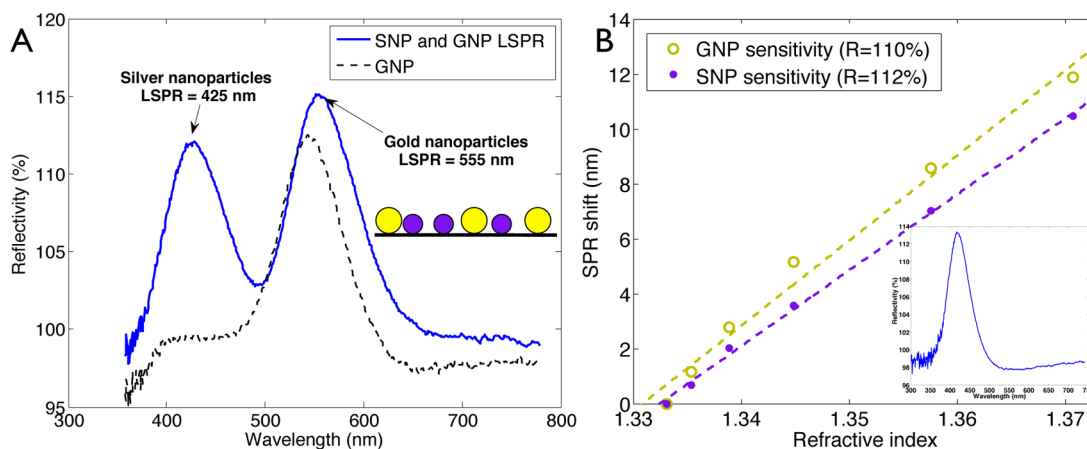


Figure 3. Multiplexed sensor. (A) Silver and gold nanoparticles LSPR bands in water at 425 and 555 nm, respectively (blue, full line), showing that overlap between the two LSPR bands is minimum and the two bands can be clearly distinguished. LSPR spectrum of GNP terminated with anti-*apoE* IgG, prior to SNP adsorption, at 545 nm (black, dotted line). (B) LSPR shift as a function of bulk refractive index for GNP or for SNP fiber samples. Sensitivity achieved with the two classes of nanoparticles is comparable. (Inset) Typical measured LSPR spectrum of SNP with a reflectivity of 112%.

index smaller than that of the medium. Observation of decreased sensitivity with higher nanoparticles density appears to be in contrast with Jain et al.,³⁶ where DDA-simulated LSPR of nanospheres pair as a function of the medium refractive index for different values of the interparticle separation is reported. The authors predict an increase in sensitivity for smaller distances. However, the scenario of many randomly positioned nanoparticles interacting is more complex than the interaction of a nanoparticle pair, where only two particles interact. From a geometrical standpoint, the effective refractive index is not affected as much as when GNPs are surrounded by other GNPs.

It is worth noticing that the sensitivity shown in Figure 2B (387 nm/RIU for the sample with $R = 102\%$) is higher than other reports (50–100 nm/RIU for spherical gold nanoparticles^{32,37}). We believe that high nanoparticle loading densities may be the cause for smaller sensitivity compared to our situation, where immobilization took place for only 5 min. For instance, the nanoparticle density measured in Nath et al.³⁷ is roughly 100 times larger than what we measured for the sample with $R = 102\%$. If we assume the trend in Figure 2B stands for larger immobilization densities, the asymptotic value of the sensitivity we expect to reach is around 80 nm/RIU. Nevertheless, the sensitivity we measured is in reasonable agreement with DDA calculation reported by Lee et al.,³⁸ which predicts a sensitivity of 331.35 nm/RIU for a 60 nm gold nanosphere. Further investigations are needed to deeply understand the reason for the higher sensitivity measured for our architecture with respect to experimental data from other authors.

However, such values are lower than those reported for SPR (above 8000 nm/RIU).^{39,40} While SPR spectroscopy provides higher sensitivity to changes in the bulk refractive index than LSPR spectroscopy, the response of the two techniques becomes comparable when measuring short-range changes in the refractive index due to a molecular adsorption layer. This is a result of the much smaller sensing volume offered by LSPR sensors, as the electromagnetic field decay length is 40–50 times shorter than that of the SPR sensors.^{23–25,41}

The bottom inset in Figure 2B shows a typical SEM image taken from a sample that had an amount of GNP

corresponding to a reflectivity of 120%. Please note that the distribution of the particles is not homogeneous, as the linking process is driven by the electrostatic attraction of the PAH layer and the Brownian motion of the GNP in solution.

The top inset of Figure 2B displays the relationship between the quantity of GNP attached to the fiber tip and the reflectivity values measured (see Experimental Section for details on data analysis). As previously mentioned, the increase of GNP density produces an increase in the reflectivity at the LSPR wavelength. The trend described by the model presented in eq 9 is displayed as well, showing a good prediction of the experimental data for low GNP density. However, for higher loading conditions, the model diverges from the experimental data, probably because images analysis becomes more difficult and the higher nanoparticle interactions affect the LSPR intensity,⁴² making the model unreliable.

Estimation of the Nanoparticle Density. From reflectivity measurements, it is possible to indirectly estimate the quantity of GNP linked to the fiber tip, taking into account the nanoparticle's physical and optical properties (scattering cross section, extinction/scattering ratio). We consider the probability that light emerging the fiber would hit a nanosphere and the proportion of the energy radiated from a nanosphere that can recouple into the fiber, taking into account the nanosphere albedo C_{alb} , a ratio of scattering to total extinction. As the light traveling through the fiber (I_0) reaches the fiber–water interface at the output cleaved of the fiber, some light is transmitted (I_t) and some is back reflected, giving rise to a background signal (B), as introduced previously

$$I_t = \alpha I_0 \quad (2)$$

$$B = (1 - \alpha)I_0 \quad (3)$$

where α is the Fresnel transmission coefficient between the fiber and the water environment, calculated using a value of 1.33 for water refractive index and 1.49 for that of the fiber.

A fraction of the transmitted light interacts with the nanoparticles (I_e), according to the scattering cross-section C_{scatt} of a single nanoparticle and the nanoparticle density N

$$I_e = \frac{C_{\text{scatt}}}{A} \iint I_t(x, y)N(x, y)dx dy \quad (4)$$

where A is the core's area. Considering the fiber is massively multimode, we could assume a top-hat intensity distribution for the transmitted light and write eq 4 as

$$I_e \approx I_t C_{\text{scatt}} \bar{N} \quad (5)$$

where \bar{N} is the nanoparticles density averaged over the whole core's area.

Some of the light is absorbed by the nanoparticles, and some is radiated over the full solid angle, depending on the optical properties of the nanoparticles used,⁴³ and can be estimated in terms of the nanosphere albedo (C_{alb}). A fraction of the scattered light is recoupled into the fiber (I_r), depending on the acceptance angle of the fiber

$$I_r = I_e C_{\text{alb}} \alpha \frac{\Omega}{4\pi} \quad (6)$$

where Ω is the acceptance solid angle to take into account the fraction of scattered light that is recoupled into the fiber

$$\Omega = 2\pi(1 - \cos \theta/2) \quad (7)$$

with θ being the acceptance angle of the fiber in water, given by its numerical aperture (NA). Dividing by the solid angle of a full sphere (4π) in eq 6 it is possible to estimate the fraction of radiated light captured by the fiber.

Combining eqs 2, 5, and 6 the light scattered by the nanoparticles and recoupled into the fiber as a function of the incident light can be approximated as

$$I_r = \alpha^2 \bar{N} C_{\text{scatt}} C_{\text{alb}} \frac{\Omega}{4\pi} I_0 \quad (8)$$

The signal measured by the spectrometer (S) is the sum of the background (B) and the scattered light coupled into the fiber I_r . Therefore, combining eq 1 with eq 8 and taking into account the relation between the background (B) and the incident light (I_0) of eq 3 the averaged nanoparticle density can be written as

$$\bar{N}(\text{particles}/\text{m}^2) = \left(\frac{R - 100}{100} \right) \times \left(\frac{1 - \alpha}{\alpha^2 \frac{\Omega}{4\pi} C_{\text{alb}} C_{\text{scatt}}} \right) \quad (9)$$

where R is the measured reflectance at the maximum of the LSPR band.

Substituting in eq 9 the values for the coefficients reported in Table 1, assuming a sample with reflectivity of 110%, we obtain

Table 1. Values of the Coefficients in Eq 9 for 80 nm GNP and for the Fiber Employed^a

C_{scatt} (m ²)	C_{alb}	α	θ	NA
1.5×10^{-14}	0.5	0.996	11°	0.258

^aValues of C_{scatt} and C_{alb} were obtained from the manufacturer spec sheet (nanoComposix).

a value for the GNP density on the sample of ~ 23 particles/ μm^2 , in reasonable agreement with the value of ~ 30 particles/ μm^2 estimated by SEM measurements (see inset in Figure 2B).

Multiplexed Sensor. Use of individual metallic nanoparticles with distinct LSPR signatures is the first step toward realization of a multiplexed dip biosensor. Then, as mentioned in the Experimental Section, by means of a functionalization protocol capable of linking different antibodies to distinct nanoparticles, each family of nanoparticles can be modified to be responsive to a specific biomarker. Furthermore, to improve

the robustness of the sensor and reduce artifacts, the LSPR band overlap must be limited. Differences in the LSPR signatures of metallic nanoparticles could come from differences in their shape, size, structure, or materials.⁴³ Here we choose to employ metallic nanoparticles made from different materials as it is an effective and straightforward means of producing LSPRs with separate bands, as presented in Figure 3A, where GNPs and SNPs are linked to the tip of the optical fiber. In Figure 3A the LSPR of SNP occurs at 425 nm and that of GNP at 555 nm.

Note that the wavelength at which GNP LSPR occurs is shifted by approximately 10 nm after adsorption of SNP on the fiber tip. This is consistent with plasmon coupling effects between adjacent nanoparticles, as previously mentioned.^{29,33} The increased reflectivity of GNP LSPR from 112.5% to 115% is due to a slight overlap with the tail of the SNP band. To illustrate the sensitivity of SNP, Figure 3B reports a comparison between the SPR shift as a function of the bulk refractive index for GNP and SNP samples. In Figure 3B a simple system (using a single class of nanoparticles) was considered, showing that the sensitivity achieved with SNPs and GNPs is comparable. Although some silver nanostructures have been reported to be more sensitive than the gold counterpart, data shown in Figure 3B are in agreement to that reported in Lee et al.³⁸ for metal nanoparticles; the bulk refractive index sensitivity of metal nanoparticles is found to be independent of material composition for metals with similar dispersion relationships in the real part of the dielectric function, as for Ag and Au.³⁸

The multiplexed system of Figure 3A was characterized as well by exposing to solutions with different refractive index, and the two LSPR bands were monitored separately. The results (see Figures S1 and S2, Supporting Information) showed a smaller sensitivity than that of the sample loaded with only one class of nanoparticles (20% smaller for SNP and 30% for GNP). This is in agreement with the data presented in Figure 2B and due to a larger overall nanoparticles density.

As far as the proposed functionalization protocol is concerned, (see Experimental Section), note that good specificity of the sensor is obtained. GNPs were modified with anti-apoE IgG until full saturation of Neutravidin binding sites is reached. Then, SNPs are linked to the fiber sample and functionalized with anti-CLU IgG following the same procedure as for GNPs. Under these experimental conditions, SNP should be free of anti-apoE antibodies while GNP might present a small amount of anti-CLU IgG if, for example, some Neutravidin binding sites are still available after introduction of anti-apoE antibodies.

Biomarker detection. To demonstrate the performances of our dip biosensor in terms of specificity, the system was exposed to a clinically relevant concentration of two gastric cancer biomarkers, as aforementioned. In a previous study, apoE and CLU were identified as potential gastric cancer biomarkers.^{44–46} The authors reported that apoE was found to be 2.5-fold overexpressed and CLU to be 2-fold underexpressed in patients with gastric cancer compared to the physiological regulation range of 36 ± 13 and 306 ± 148 $\mu\text{g}/\text{mL}$ respectively. Therefore, we tested the dip biosensor by exposing the surface to solutions of the two biomarkers, 90 $\mu\text{g}/\text{mL}$ for apoE and 160 $\mu\text{g}/\text{mL}$ for CLU, and analyzing the two LSPR bands separately and simultaneously.

The biosensor was first dipped into the solution containing apoE, and the wavelength positions of the two LSPR bands were monitored separately (see data analysis section for

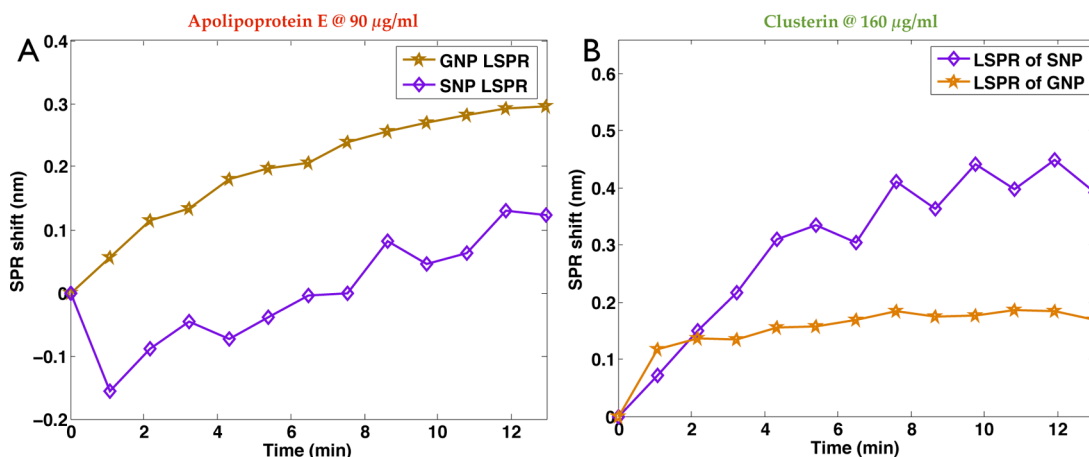


Figure 4. Dip biosensing of gastric cancer biomarkers. (A) Shift of the LSPR bands upon exposure of the biosensor to a 90 µg/mL solution of apoE. Star curve represents the real-time shift of the GNP LSPR band, while diamond curve is the shift of the SNP LSPR band. Note that only the surface of GNP is functionalized with anti-apoE antibody. (B) Shift of the LSPR bands upon immersion in a 160 µg/mL solution of CLU. Diamond line represents the SNP band, while star line represents the GNP band. Note that for the biosensing experiments a volume as small as 25 µL was added into an Eppendorf tube, where the fiber sample was later dipped.

details). Results are presented in Figure 4A, where the diamond symbols represent the shift of the LSPR band corresponding to SNP (at 425 nm) while the stars represent that corresponding to GNP (band at 555 nm). From the figure we can state that GNP are clearly responsive to apoE, producing a neat shift of 0.3 nm in less than 15 min. Regarding the signal from SNP, an overall shift of 0.1 nm is obtained, probably due to a degree of nonspecific binding, but the shift measured is 3 times smaller than that for GNP. The sensor was then dipped in the vial containing the CLU solution. The response for the two LSPR bands is presented in Figure 4B. In this case a shift of 0.4 nm for the LSPR band corresponding to SNP is measured (diamond line), consistent with the functionalization employed, proving that SNP are responsive principally to CLU. A small shift is also observable for the LSPR of GNP, but it is in magnitude smaller than that observed for SNP. This set of biosensing experiments contains also the negative (or control) test, demonstrating the specificity of the system proposed. In fact, Figure 4 demonstrates that the functionalized SNP nanoparticles are principally receptive toward CLU while GNP toward apoE. The shift measured when the wrong target is present is roughly 3 times smaller than that shift arising as a consequence of the target recognition, proving also that the functionalization approach employed was successful. It is worth noting that although the shift observed here is rather small, the resolution of the sensor, which depends on the equipment and data analysis employed, allow us to discriminate a SPR shift (Res) of 0.03 nm, calculated as three times the noise.^{14,47} The resolution is strictly connected to the limit of detection, which is often reported as a means to measure the performance of a sensor, which is not an intrinsic characteristic of the sensor because it depends also on the equipment used to measure it.

Note that the magnitude of the shift measured is consistent with the magnitude of the shifts observed during the functionalization process (see Figures S3 and S4, Supporting Information). However, it is important to point out that the sensitivity of the sensor decreases as a function of the functionalization steps, because the electromagnetic field decays exponentially from the nanoparticles surface, thus limiting the sensing volume.^{23,48,49} In particular, assuming an electromagnetic field decay of 20–50 nm⁴⁹ and considering a

functionalization shell (ssDNA-NAVD-IgG) thickness of roughly 20–25 nm, the interaction between the electromagnetic field and the analyte (apoE and CLU) is reduced with respect to the situation of the analyte being adsorbed directly on the nanoparticles surface, thus resulting in smaller LSPR shifts. However, considering that the shift observed for apoE IgG (150 kDa) immobilization is roughly 1.2 nm (see Figure S3, Supporting Information) and taking into account that the molecular weight of apoE is around 30 kDa, the shift observed upon apoE exposure (~0.3 nm) is consistent with the shift measured for apoE antibody, assuming a 1:1 ratio of proteins captured per IgG. In the case of CLU (70 kDa), taking into account the relative molecular weight and the LSPR shift measured (see Figure S4, Supporting Information), a ratio of one CLU per two IgG is obtained. This could be caused to a smaller binding affinity or IgG degradation.

Note also that the protein's solution volume employed for the dip biosensing experiments is as small as 25 µL, and it could be further reduced, proving the powerfulness of such a system for low-cost biomarkers screening.

Nanoparticle Positioning. The surface chemistry in the sensing region has a substantial impact on the performance of biosensors as it drives the interactions of light with biomolecules at the nanoscale, and it could be used to improve the sensor performance as well as introduce features not present otherwise. Here we report a previously unobserved behavior for colloidal nanoparticles that occurs during SNP anchorage to the surface that is due to modification of the surface chemistry of the nanoparticles, which allows for manipulation of their positioning during adsorption.

Adsorption is driven by the electrostatic interactions between the positively charged surface and the negatively charged metallic nanoparticles (see Experimental Section). After adsorption and functionalization of GNP, SNP linkage took place in the same manner by electrostatic interaction with the positively charged surface, causing consistently an overall red shift of 10 nm on the GNP LSPR band. We attributed this fact to the increased density of nanoparticles, thus leading to a smaller interparticles average distance, as well known for the system where only one class of nanoparticles (GNP for instance) is interacting.³³ In a different set of experiments, we

modified GNP surface to introduce a positive surface charge, by reacting with a solution of 1 mM 11-amino-1-undecanethiol in ethanol, that forms self-assembled monolayers (SAM) on the surface of GNP.⁵⁰ After introduction of such positive charge on the surface of GNP, SNP were deposited following the same protocol previously reported. However, in this situation SNP can adsorb both to the fiber surface and to the positively charged GNP. As a result, a blue shift of the GNP LSPR band was consistently observed, in contrast with experimental observations reported for interacting colloidal nanoparticles^{33,51} and with results presented above.

Experimental evidence of this effect is given in Figure 5, where a blue shift of 4 nm is observed as well as the appearance

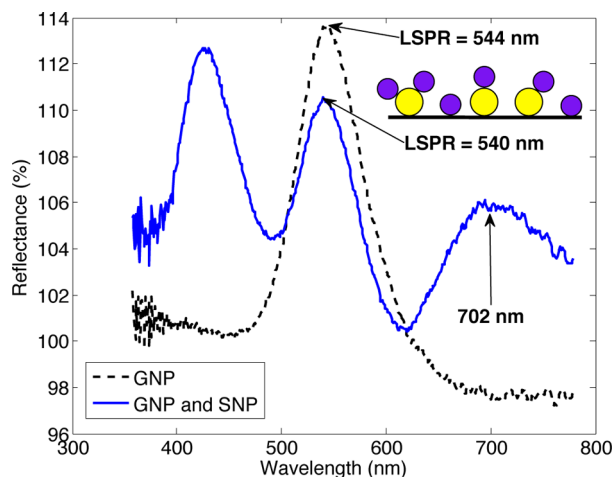


Figure 5. Multiplexed sensor. Silver and gold nanoparticles LSPR bands in water at 426 and 540 nm, respectively (blue, full line). LSPR of GNP before SNP deposition, at 544 nm (black, dotted line). Blue shift is observed for the GNP LSPR band after immobilization of SNP, in contrast with what is observed in Figure 3A. (Inset) Cartoon depicting SNP disposition on GNP, thanks to the positively charged surface.

of a third band at 700 nm, probably coming from a combined mode. This effect may be related to the SNPs attaching to GNPs via the SAM linker. Note that for the plasmonic coupling to take effect the polarization of the electromagnetic field needs to be parallel to the interparticles direction, as for the case of SNP lying on the plane of the fiber tip with GNP (see cartoon in Figure 3A, inset). In the situation where SNPs lie on top of GNPs, as depicted in the cartoon in the inset of Figure 5, the polarization of electromagnetic field (which lies in the fiber tip plane) is perpendicular to the GNP–SNP direction and thus unable to cause a plasmonic coupling between the GNP and the SNP, resulting in significantly different behavior. Similar behavior was reported by other authors^{42,52} for two interacting gold nanodisks deposited by E-B lithography, where a blue shift in the case of polarization orthogonal to the long particle pair axis was observed as the interparticle distance decreased. The given interpretation relies on the dipole–dipole interaction model, showing that the charge distributions of both particles act cooperatively to enhance the repulsive action of surface charges, thus increasing the resonance frequency. Also, it is interesting to note the relative intensity change in the GNP LSPR, which decreases in the case of Figure 5 but increases in Figure 3A. This is in agreement with the dipolar-coupling picture, as reported in Huang et al.,⁴² and supports our

interpretation of a different nanoparticles positioning driven by surface functionalization.

For our experimental conditions there may be an additional effect that adds to what has been already described, connected to the local effective refractive index, which affects also the position of GNP's LSPR. In fact, the real part of the refractive index of silver is significantly below that of water in the optical regime, and the presence of SNP on top of GNP simply reduces the local effective refractive index, producing a blue shift of the GNP's LSPR, in accordance with experimental observations. In a more general case, there will be a degree of coupling between the SNPs and the GNPs, depending on the relative positions of the nanoparticles and light polarization. The results show how, by playing with surface functionalization, it is possible to tailor interactions of nanoparticles with surfaces and interactions among nanoparticles, adding extra degrees of freedom to nanophotonics and plasmonics, without the need for nanofabrication.

CONCLUSION

We report a dip biosensor based on anchoring metallic nanoparticles to the tip of a cleaved optical fiber. Localized surface plasmons are excited by the light traveling in the fiber and are responsible as the transduction mechanism for the refractometric biosensor presented. We explored the impact of the nanoparticle density on the sensor performance, demonstrating that smaller quantities of nanoparticles lead to better sensitivity. By linking nanoparticles with different plasmonic signatures and employing a suitable functionalization strategy, a multiplexed biosensor is realized. The dip biosensor is proven to be effective in detecting two different gastric cancer biomarkers in clinically relevant conditions simultaneously with a limited cross-reactivity and in a short time frame (~10 min). Furthermore, a minimum volume of solution is required both for the functionalization process and for sample analysis, dramatically reducing the costs associated with POCT. There are possibilities for the system to be improved, as, for instance, via the use of core–shell nanoparticles.⁴³ By employing such nanoparticles it should be possible to design and tailor the plasmonic features to have LSPR bands in any desired position, enabling the system to be engineered to detect a larger number of biomarkers, making this new sensing platform extremely attractive for applications in medical diagnostics.

ASSOCIATED CONTENT

Supporting Information

Characterization data of the multiplexed sensor as a function of the refractive index; LSPR kinetics for the multiplexed sensor during immobilization of apoE and CLU IgG. This material is available free of charge via the Internet at <http://pubs.acs.org>.

AUTHOR INFORMATION

Corresponding Authors

*E-mail: beni.sciacca@gmail.com.

*E-mail: tanya.monro@adelaide.edu.au.

Notes

The authors declare no competing financial interest.

ACKNOWLEDGMENTS

The authors acknowledge the support of NHMRC Grant APP1010728 and useful conversations with Peter Hoffmann and Alexandre Francois. T.M. acknowledges an ARC Laureate

Fellowship. Surface functionalisation facilities were provided within the OptoFab node of the Australian National Fabrication Facility utilizing Commonwealth and SA State Government funding.

REFERENCES

- (1) Basso, W.; Hartnack, S.; Pardini, L.; Maksimov, P.; Koudela, B.; Venturini, M. C.; Schares, G.; Sidler, X.; Lewis, F. I.; Deplazes, P. Assessment of diagnostic accuracy of a commercial ELISA for the detection of *Toxoplasma gondii* infection in pigs compared with IFAT, TgSAG1-ELISA and Western blot, using a Bayesian latent class approach. *Int. J. Parasitol.* **2013**, *43*, 565–570.
- (2) Guidi, A.; Laricchia-Robbio, L.; Gianfaldoni, D.; Revoltella, R.; Del Bono, G. Comparison of a conventional immunoassay (ELISA) with a surface plasmon resonance-based biosensor for IGF-1 detection in cows' milk. *Biosens. Bioelectron.* **2001**, *16* (9–12), 971–977.
- (3) Campbell, K.; Huet, A. C.; Charlier, C.; Higgins, C.; Delahaut, P.; Elliott, C. T. Comparison of ELISA and SPR biosensor technology for the detection of paralytic shellfish poisoning toxins. *J. Chromatogr., B: Anal. Technol. Biomed. Life Sci.* **2009**, *877* (32), 4079–4089.
- (4) Louie, R. F.; Tang, Z. P.; Shelby, D. G.; Kost, G. J. Point-of-care testing: Millennium technology for critical care. *Lab. Med.* **2000**, *31* (7), 402–408.
- (5) Soper, S. A.; Brown, K.; Ellington, A.; Frazier, B.; Garcia-Manero, G.; Gau, V.; Gutman, S. I.; Hayes, D. F.; Korte, B.; Landers, J. L.; Larson, D.; Ligler, F.; Majumdar, A.; Mascini, M.; Nolte, D.; Rosenzweig, Z.; Wang, J.; Wilson, D. Point-of-care biosensor systems for cancer diagnostics/prognostics. *Biosens. Bioelectron.* **2006**, *21* (10), 1932–1942.
- (6) Holford, T. R. J.; Davis, F.; Higson, S. P. J. Recent trends in antibody based sensors. *Biosens. Bioelectron.* **2012**, *34* (1), 12–24.
- (7) Vasan, A. S.; Mahadeo, D. M.; Doraiswami, R.; Huang, Y.; Pecht, M. Point-of-care biosensor system. *Front. Biosci., Scholar Ed.* **2013**, *5*, 39–71.
- (8) Gimzewski, J.; Reed, J.; Teitell, M.; Malan, G. 15 Immunological Biosensors. In *The Immunoassay Handbook*, 4th ed.; Wild, D., Ed.; Elsevier: New York, 2013.
- (9) Wang, J. Electrochemical glucose biosensors. *Chem. Rev.* **2008**, *108* (2), 814–25.
- (10) Poolsup, N.; Suksomboon, N.; Rattanasookchit, S. Meta-analysis of the benefits of self-monitoring of blood glucose on glycemic control in type 2 diabetes patients: an update. *Diabetes Technol. Ther.* **2009**, *11* (12), 775–84.
- (11) Skeie, S.; Kristensen, G. B.; Carlsen, S.; Sandberg, S. Self-monitoring of blood glucose in type 1 diabetes patients with insufficient metabolic control: focused self-monitoring of blood glucose intervention can lower glycated hemoglobin A1C. *J. Diabetes Sci. Technol.* **2009**, *3* (1), 83–8.
- (12) Mascini, M.; Tombelli, S. Biosensors for biomarkers in medical diagnostics. *Biomarkers* **2008**, *13* (7–8), 637–657.
- (13) Fan, X. D.; White, I. M.; Shopova, S. I.; Zhu, H. Y.; Suter, J. D.; Sun, Y. Z. Sensitive optical biosensors for unlabeled targets: A review. *Anal. Chim. Acta* **2008**, *620* (1–2), 8–26.
- (14) Sciacca, B.; Francois, A.; Klingler-Hoffmann, M.; Brazzatti, J.; Penno, M.; Hoffmann, P.; Monro, T. M. Radiative-surface plasmon resonance for the detection of apolipoprotein E in medical diagnostics applications. *Nanomedicine* **2012**, *9*, 550–557.
- (15) Francois, A.; Boehm, J.; Oh, S. Y.; Kok, T.; Monro, T. M. Collection mode surface plasmon fibre sensors: A new biosensing platform. *Biosens. Bioelectron.* **2011**, *26* (7), 3154–3159.
- (16) Bhatta, D.; Michel, A. A.; Marti Villalba, M.; Emmerson, G. D.; Sparrow, I. J.; Perkins, E. A.; McDonnell, M. B.; Ely, R. W.; Cartwright, G. A. Optical microchip array biosensor for multiplexed detection of bio-hazardous agents. *Biosens. Bioelectron.* **2011**, *30* (1), 78–86.
- (17) Liu, G.; Lao, R.; Xu, L.; Xu, Q.; Li, L.; Zhang, M.; Song, S.; Fan, C. Single-nucleotide polymorphism genotyping using a novel multiplexed electrochemical biosensor with nonfouling surface. *Biosens. Bioelectron.* **2012**, *42*, 516–21.
- (18) Qureshi, A.; Niazi, J. H.; Kallemudi, S.; Gurbuz, Y. Label-free capacitive biosensor for sensitive detection of multiple biomarkers using gold interdigitated capacitor arrays. *Biosens. Bioelectron.* **2010**, *25* (10), 2318–2323.
- (19) Scarano, S.; Mascini, M.; Turner, A. P. F.; Minunni, M. Surface plasmon resonance imaging for affinity-based biosensors. *Biosens. Bioelectron.* **2010**, *25* (5), 957–966.
- (20) Sciacca, B.; Francois, A.; Hoffmann, P.; Monro, T. M. Multiplexing of radiative-surface plasmon resonance for the detection of gastric cancer biomarkers in a single optical fiber. *Sens. Actuators, B* **2013**, *183*, 454–458.
- (21) Chang, Y. F.; Yu, J. S.; Chang, Y. T.; Su, L. C.; Wu, C. C.; Chang, Y. S.; Lai, C. S.; Chou, C. The utility of a high-throughput scanning biosensor in the detection of the pancreatic cancer marker ULBP2. *Biosens. Bioelectron.* **2013**, *41*, 232–237.
- (22) Cork, J.; Jones, R. M.; Sawyer, J. Low cost, disposable biosensors allow detection of antibodies with results equivalent to ELISA in 15 min. *J. Immunol. Methods* **2013**, *387* (1–2), 140–146.
- (23) Mayer, K. M.; Hafner, J. H. Localized Surface Plasmon Resonance Sensors. *Chem. Rev.* **2011**, *111* (6), 3828–3857.
- (24) Anker, J. N.; Hall, W. P.; Lyandres, O.; Shah, N. C.; Zhao, J.; Van Duyne, R. P. Biosensing with plasmonic nanosensors. *Nat. Mater.* **2008**, *7* (6), 442–453.
- (25) Sagle, L. B.; Ruvuna, L. K.; Ruellemele, J. A.; Van Duyne, R. P. Advances in localized surface plasmon resonance spectroscopy biosensing. *Nanomedicine* **2011**, *6* (8), 1447–1462.
- (26) Mitsui, K.; Handa, Y.; Kajikawa, K. Optical fiber affinity biosensor based on localized surface plasmon resonance. *Appl. Phys. Lett.* **2004**, *85* (18), 4231–4233.
- (27) Lee, J. Y.; Lee, C. W.; Lin, E. H.; Wei, P. K. Single live cell refractometer using nanoparticle coated fiber tip. *Appl. Phys. Lett.* **2008**, *93* (17).
- (28) Yi, J. H.; Jao, C. Y.; Kandas, I. L. N.; Liu, B.; Xu, Y.; Robinson, H. D. Irreversible adsorption of gold nanospheres on fiber optical tapers and microspheres. *Appl. Phys. Lett.* **2012**, *100* (15).
- (29) Sonnichsen, C.; Reinhard, B. M.; Liphardt, J.; Alivisatos, A. P. A molecular ruler based on plasmon coupling of single gold and silver nanoparticles. *Nat. Biotechnol.* **2005**, *23* (6), 741–745.
- (30) Zhang, X.; Servos, M. R.; Liu, J. Instantaneous and quantitative functionalization of gold nanoparticles with thiolated DNA using a pH-assisted and surfactant-free route. *J. Am. Chem. Soc.* **2012**, *134* (17), 7266–9.
- (31) Laitinen, O. H.; Hytonen, V. P.; Nordlund, H. R.; Kulomaa, M. S. Genetically engineered avidins and streptavidins. *Cell. Mol. Life Sci.* **2006**, *63* (24), 2992–3017.
- (32) Sun, Y. G.; Xia, Y. N. Increased sensitivity of surface plasmon resonance of gold nanoshells compared to that of gold solid colloids in response to environmental changes. *Anal. Chem.* **2002**, *74* (20), 5297–5305.
- (33) Jain, P. K.; Huang, W. Y.; El-Sayed, M. A. On the universal scaling behavior of the distance decay of plasmon coupling in metal nanoparticle pairs: A plasmon ruler equation. *Nano Lett.* **2007**, *7* (7), 2080–2088.
- (34) Reinhard, B. M.; Siu, M.; Agarwal, H.; Alivisatos, A. P.; Liphardt, J. Calibration of dynamic molecular rulers based on plasmon coupling between gold nanoparticles. *Nano Lett.* **2005**, *5* (11), 2246–52.
- (35) Funston, A. M.; Novo, C.; Davis, T. J.; Mulvaney, P. Plasmon Coupling of Gold Nanorods at Short Distances and in Different Geometries. *Nano Lett.* **2009**, *9* (4), 1651–1658.
- (36) Jain, P. K.; El-Sayed, M. A. Noble Metal Nanoparticle Pairs: Effect of Medium for Enhanced Nanosensing. *Nano Lett.* **2008**, *8* (12), 4347–4352.
- (37) Nath, N.; Chilkoti, A. A colorimetric gold nanoparticle sensor to interrogate biomolecular interactions in real time on a surface. *Anal. Chem.* **2002**, *74* (3), 504–509.
- (38) Lee, K. S.; El-Sayed, M. A. Gold and silver nanoparticles in sensing and imaging: Sensitivity of plasmon response to size, shape, and metal composition. *J. Phys. Chem. B* **2006**, *110* (39), 19220–19225.

(39) Jung, L. S.; Campbell, C. T.; Chinowsky, T. M.; Mar, M. N.; Yee, S. S. Quantitative interpretation of the response of surface plasmon resonance sensors to adsorbed films. *Langmuir* **1998**, *14* (19), 5636–5648.

(40) Abbas, A.; Linman, M. J.; Cheng, Q. A. New trends in instrumental design for surface plasmon resonance-based biosensors. *Biosens. Bioelectron.* **2011**, *26* (5), 1815–1824.

(41) Willets, K. A.; Van Duyne, R. P. Localized surface plasmon resonance spectroscopy and sensing. *Annu. Rev. Phys. Chem.* **2007**, *58*, 267–97.

(42) Huang, W. Y.; Qian, W.; Jain, P. K.; El-Sayed, M. A. The effect of plasmon field on the coherent lattice phonon oscillation in electron-beam fabricated gold nanoparticle pairs. *Nano Lett.* **2007**, *7* (10), 3227–3234.

(43) Jain, P. K.; Lee, K. S.; El-Sayed, I. H.; El-Sayed, M. A. Calculated absorption and scattering properties of gold nanoparticles of different size, shape, and composition: applications in biological imaging and biomedicine. *J. Phys. Chem. B* **2006**, *110* (14), 7238–48.

(44) Liu, W. T.; Liu, B. Y.; Cai, Q.; Li, J. F.; Chen, X. H.; Zhu, Z. G. Proteomic identification of serum biomarkers for gastric cancer using multi-dimensional liquid chromatography and 2D differential gel electrophoresis. *Clin. Chim. Acta* **2012**, *413* (13–14), 1098–1106.

(45) Sakashita, K.; Tanaka, F.; Zhang, X.; Mimori, K.; Kamohara, Y.; Inoue, H.; Sawada, T.; Hirakawa, K.; Mori, M. Clinical significance of ApoE expression in human gastric cancer. *Oncol. Rep.* **2008**, *20* (6), 1313–1319.

(46) Penno, M. A.; Klingler-Hoffmann, M.; Brazzatti, J. A.; Boussioutas, A.; Putoczki, T.; Ernst, M.; Hoffmann, P. 2D-DIGE analysis of sera from transgenic mouse models reveals novel candidate protein biomarkers for human gastric cancer. *J. Proteomics* **2012**, *77*, 40–58.

(47) Shevchenko, Y.; Francis, T. J.; Blair, D. A. D.; Walsh, R.; DeRosa, M. C.; Albert, J. In Situ Biosensing with a Surface Plasmon Resonance Fiber Grating Aptasensor. *Anal. Chem.* **2011**, *83* (18), 7027–7034.

(48) Haes, A. J.; Zou, S. L.; Schatz, G. C.; Van Duyne, R. P. Nanoscale optical biosensor: Short range distance dependence of the localized surface plasmon resonance of noble metal nanoparticles. *J. Phys. Chem. B* **2004**, *108* (22), 6961–6968.

(49) Malinsky, M. D.; Kelly, K. L.; Schatz, G. C.; Van Duyne, R. P. Chain length dependence and sensing capabilities of the localized surface plasmon resonance of silver nanoparticles chemically modified with alkanethiol self-assembled monolayers. *J. Am. Chem. Soc.* **2001**, *123* (7), 1471–1482.

(50) Love, J. C.; Estroff, L. A.; Kriebel, J. K.; Nuzzo, R. G.; Whitesides, G. M. Self-assembled monolayers of thiolates on metals as a form of nanotechnology. *Chem. Rev.* **2005**, *105* (4), 1103–69.

(51) Ghosh, S. K.; Pal, T. Interparticle coupling effect on the surface plasmon resonance of gold nanoparticles: from theory to applications. *Chem. Rev.* **2007**, *107* (11), 4797–862.

(52) Rechberger, W.; Hohenau, A.; Leitner, A.; Krenn, J. R.; Lamprecht, B.; Aussenegg, F. R. Optical properties of two interacting gold nanoparticles. *Opt. Commun.* **2003**, *220* (1–3), 137–141.